Evidence of Structure-Performance Relation for Surfactants used as Anti-Agglomerants for Hydrates Management

Tai Bui[#], Anh Phan[#], Deepak Monteiro, Qiang Lan, Mark Ceglio, Erick Acosta[+], Pushkala Krishnamurthy[+] and Alberto Striolo[#]

[#] Department of Chemical Engineering, University College London, WC1 E7JE London, UK
[+] Halliburton, Houston, Texas, USA

Abstract

Molecular dynamics simulations were employed to study the structure of molecularly-thin films of anti-agglomerants adsorbed at the interface between sII methane hydrates and a liquid hydrocarbon. The liquid hydrocarbon was composed of dissolved methane and higher molecular weight alkane such as n-hexane, n-octane, or n-dodecane. The anti-agglomerants considered were surface-active compounds with three hydrophobic tails and a complex hydrophilic head that contains both amide and tertiary ammonium cation groups. The length of the hydrophobic tails and the surface density of the compounds were changed systematically. The results were analyzed in terms of the preferential orientation of the anti-agglomerants, density distributions of various molecular compounds, and other molecular-level properties. At low surface densities the hydrophobic tails do not show preferred orientation, irrespectively of the tail length. At sufficiently high surface densities, our simulations show pronounced differences in the structure of the interfacial film depending on molecular features and on the type of the hydrocarbons present in the system. Some anti-agglomerants are found to pack densely at the interface and exclude methane from the interfacial region. At these conditions the anti-agglomerants film resembles a 'frozen interface'. The hydrophobic tails of the anti-agglomerants that show this feature are of length comparable to that of the n-dodecane in the liquid phase. It is possible that the structured interfacial layer is in part responsible for determining the performance of anti-agglomerants in flow-assurance applications. The simulation results are qualitatively compared against experimental data obtained with the rocking cell apparatus. It was found that the anti-

agglomerants for which our simulations suggest evidence of frozen interface at sufficiently high surface densities are those that show better performance in rocking cell experiments.

INTRODUCTION

Gas hydrates are inclusion compounds formed by hydrogen-bonded water cages stabilized by small guest gas molecules. They are formed at high pressure and low temperature conditions.[1] Gas hydrates are considered as both a potential energy source and a method to trap carbon dioxide,[2] although environmental aspects need to be carefully assessed.[3, 4] Gas hydrates are known to, under appropriate conditions, block pipelines,[1, 5] which affects negatively the oil and gas production, with important safety and environmental consequences.[1, 6]

Chemicals, known as hydrate inhibitors, are often used to prevent hydrates from plugging pipelines,[7, 8] i.e., in the flow assurance application. Hydrates inhibitors are differentiated depending on their mode of action: Thermodynamic Inhibitors (THIs) shift the hydrate formation conditions to lower temperatures and higher pressures. Large concentrations of THIs are required (up to 20-50 % by weight of total water) to ensure performance.[9] Low Dosage Hydrate Inhibitors (LDHIs) instead function at low concentrations. Among LDHIs are Kinetic Hydrate Inhibitors (KHIs)[10, 11] and Anti-Agglomerants (AAs).[12, 13] Most of KHIs are polymers containing amide groups, such as poly(N-vinyl pyrrolidone),[10] polyvinyl-caprolactam, polydiethylacrylamide.[9] They are believed to affect the hydrogen-bonding network of water and thus delay the formation of hydrates. AAs allow the formation of hydrates but prevent small hydrate particles from agglomerating and sticking to the pipe wall. AAs are usually amphiphilic chemicals with complex hydrophobic tails and hydrophilic head groups. Because of their amphiphilic nature, these compounds are surface active, and as such they adsorb at water-oil and hydrate-oil interfaces. Several studies[1, 9, 13] indeed suggest that the AAs adsorption on hydrate surfaces is one of the mechanisms that could help preventing hydrates agglomeration. Shell patented ammonium salts surfactants to be used as AAs.[14] While AAs can perform well even at high sub-cooling conditions, their performance in general requires a liquid hydrocarbon phase. To prevent hydrates agglomeration, the AAs should affect the effective attractive interactions between hydrate particles. According to Aman et al.,[15] the three main mechanisms responsible for cohesive forces between hydrate particles are: (1) solid-solid attraction between two hydrate particles, (2) capillary attraction,[16] when a water bridge connects two hydrate particles, and (3) hydrate growth or sintering. When AAs adsorb at the oil-hydrate interface, the hydrophobic tails preferably point towards the hydrocarbon phase possibly inducing an effective repulsion when two hydrates approach each other.[1, 15, 17] When the AAs polar head groups is adsorbed on the hydrate surface, it could interfere with the hydrate growth process reducing the growing rate.[13] Other possible mechanisms by which AAs may reduce cohesive forces between hydrate particles include their ability to lower oil-water interfacial tension and/or to prevent hydrate growth within the water bridge during sintering of two hydrate particles. While many mechanisms have been proposed, the molecular mechanism that determines AAs performance is not fully understood, despite a large number of experiments reported in the literature.[12, 14, 18-20] It is of particular interest that small changes in the AAs molecular features often yield dramatic changes in performance. It is possible that these observations are due to changes in the molecular structure of AAs films adsorbed at hydrate-oil interfaces.

In an attempt to clarify the AAs action mechanism, we employed molecular dynamics simulations to quantify and visualize the molecular structure of AAs adsorbed on hydrate surfaces. We systematically changed the AAs surface density and their molecular features, including in our study compounds that show acceptable and poor performance in applications. Unfortunately, for the AAs simulated here adsorption isotherms measured on either hydrates or water-oil interfaces are not available. For comparison purposes, it has been reported that simple single-tail or gemini surfactants adsorb with surface densities as high as 2.5 molecules per nm^2.[21, 22] Because the AAs considered here are much more complex, and certainly bulkier than single-tailed surfactants, the maximum surface density they can achieve must be somewhat lower. The maximum surface density considered in our simulations was of 0.89 molecules per nm^2. The AAs selected for the simulation have been tested for their sII hydrate dispersion performance by laboratory rocking cell evaluations. The experimental results indicate that a certain combination of length of the carbon chain at head and tail is important for rocking cell performance. Rocking cells are PVT cells used by the industry to visually observe the performance of AA's for specific field conditions. The system parameters that describe the simulated systems (hydrate type, sII, pressure, temperature, fluid composition, AAs structures) were chosen to replicate experimentally relevant conditions.

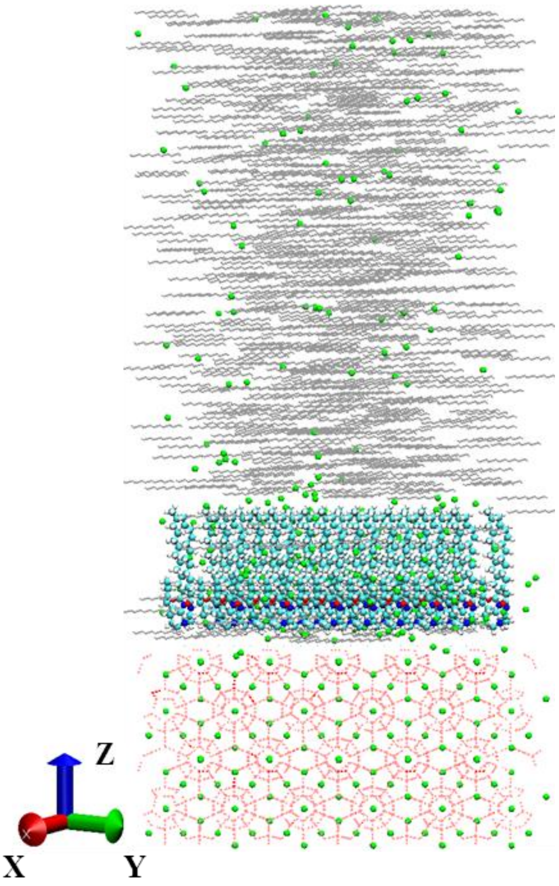

Figure 1. Initial configuration for a system composed of 24 AAs molecules. Red dotted lines represent water molecules in the hydrate substrate. Green spheres and silver lines represent methane and n-dodecane molecules, respectively. Yellow, red, blue, white, and cyan spheres represent chloride ions, oxygen, nitrogen, hydrogen and carbon atoms in AA molecules, respectively.

SIMULATION METHODOLOGY

Molecular dynamics (MD) simulations were performed by using the GROMACS simulation package,[23, 24] version 5.0.4.

In all simulations sII hydrates were considered as the solid substrate. Anti-agglomerants (AAs), chloride counter-ions, n-dodecane, and methane composed the liquid phase. To construct the initial configurations, one unit cell of sII methane hydrates was adopted from the study of Takeuchi et al.[25] The positions of the water oxygen atoms were obtained from the analysis of X-ray diffraction experimental data. The coordinates of the water hydrogen atoms were determined from MD simulation conducted with the constraint of satisfying the ice rules with zero net dipole moment at the lowest potential energy.

Although the sII methane hydrate is thermodynamically stable at high pressure conditions (> 100 MPa),[26, 27] at moderate pressure and temperature conditions it is expected that sI and sII methane hydrates coexist, as confirmed by experiments[28] (similar results were reported for CO_2 hydrates)[29, 30] and simulations.[31] In the literature, sII methane hydrates were employed to study hydrate growth[32] as well as the interaction between fragments of LDHIs and hydrates using MD simulations.[33] The sII methane hydrate was chosen for the present study because it is expected to represent the hydrate formed during the experiments, which are discussed below. The underlying assumption is that the host gas would not affect the properties of the AAs film, which is the subject matter of this investigation. We confirmed that the sII hydrate remained intact within the time frame of our MD simulations by analyzing order parameters and other structural features. The details are discussed in Figure S1 in the Supplemental Material (SM). The investigation of the relative stability of sI vs. sII hydrates at the conditions simulated here is beyond the scopes of the manuscript.

The sII methane hydrate unit cell was replicated 3 times in the X, Y directions (5.193 nm) and 2 times in the Z direction (3.462 nm). Because all-atom molecular dynamics cannot at present describe the process of surfactants adsorption on a hydrate (which occurs in time scales of the order of microseconds), the desired number of AAs molecules was arranged near the hydrate substrate. The chloride counter-ions (Cl^-) were placed next to the AAs head groups. N-dodecane and methane molecules, with molar ratio 10:3, were placed within the remainder of the simulation box. One representative initial configuration is shown in **Error! Reference source not found.**. The compositions of all simulated systems are summarized in **Table 1**. Note that although the experiments were conducted in the presence of Green Canyon gas (see experimental section below), the composition of the gas is for the most part methane. Simulating ethane and propane in a mole fraction correspondent to that of the experimental systems would require simulation boxes too large given the current computational capabilities.

To remove high-energy configurations, an energy minimization simulation was conducted from the initial configurations implementing the steepest descent method. Subsequently, to minimize the possibility that the initial configurations biased the simulation results, a NVT temperature-annealing procedure, as implemented in GROMACS, was conducted. The algorithm linearly decreased the system temperature from 1000 K to 277 K in 500 ps. In these simulations the hydrate substrate and chloride ions were maintained frozen. Subsequently, the equilibration phase was conducted within the NPT ensemble at thermodynamic conditions favorable for hydrate formation[34] (T = 277 K and P = 20 MPa). These conditions were chosen because consistent with the experiments we considered. The pressure coupling was only applied along the Z direction of the simulation box, which allowed us to maintain X and Y dimensions constant, and keep the same surface area for different systems. Temperature and pressure were maintained constant at 277 K and 20 MPa, respectively, using the Berendsen thermostat and barostat for 2 ns. This is considered the most efficient algorithm to scale simulation boxes at the beginning of a simulation.[35] After 2 ns we switched to the Nose-Hoover thermostat and the Parrinello-Rahman barostat, which are considered more thermodynamically-consistent algorithms.[35] In the NPT simulations all molecules in the system were allowed to move, even water and methane molecules in hydrate layer. Each NPT simulation was run for at least 50 ns. To ensure equilibration was reached, we evaluated the convergence of total energy and system density as well as density profiles of methane along the Z direction of the simulation box (see Figure S2, S3, S4 of the Supplemental Material for more details). Once equilibration was achieved, a 10 ns production run was conducted in the NPT ensemble at T=277 K and P=20 MPa using Nose-Hoover thermostat and the Parrinello-Rahman barostat, with pressure coupling along the Z direction of the simulation box. The results obtained during the production run were analyzed and are presented below.

The TIP4P/Ice model[36] was implemented to simulate water molecules. By using the TIP4P/Ice model, Conde and Vega[37] found that the equilibrium temperature for the formation of gas hydrates at high pressure was close to the experimental value. This model is widely and successfully implemented to study hydrate nucleation and growth,[31, 38] as well as to investigate the performance of potential hydrate inhibitors.[39] Methane and n-dodecane were represented within the united-atom version of the TraPPE-UA force field.[40]

The AA molecular structure is shown in **Figure 2**. In this figure the two R_1 groups represent ‘long’ tails, and R_2 represents a ‘short’ tail. All AA molecules in our study have the same head group, which includes both amide and tertiary ammonium cation groups, and have alkyl tails of varying length. In our notation, an AA is represented by S_XL_Y where X and Y indicate the number of carbon atoms in the short (S) and long (L) tails. Four AAs were simulated: S_4L_8, S_4L_{12}, S_6L_{12}, and S_8L_{12}. The long tails considered are either n-octyl (in S_4L_8) or n-dodecyl (in S_4L_{12}, S_6L_{12} and S_8L_{12}), while the short tails considered are n-butyl (in S_4L_8 and S_4L_{12}), n-hexyl (in S_6L_{12}), or n-octyl (in S_8L_{12}). AAs were modelled by using the General Amber Force Field (GAFF), which is often implemented for modeling organic and pharmaceutical molecules containing H, C, N, O, S, P and halogens.[41] Atomic charges were calculated with the AM1-BCC method employed in Antechamber from the Amber 14 suite.[42] The chloride ions (Cl^-) were modeled as charged Lennard-Jones spheres with the potential parameters taken from Dang, without polarizability. [43]

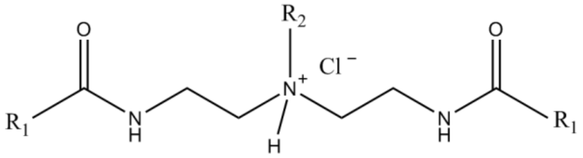

Figure 2. Molecular structure of AAs with two long tails R_1 (n-octyl for S_4L_8 and n-dodecyl for S_4L_{12}, S_6L_{12} AAs) and one short tail R_2 (n-butyl for S_4L_8, S_4L_{12}; n-hexyl forS_6L_{12}, and n-octyl for S_8L_{12} AAs).

Dispersive and electrostatic forces were modeled by the 12-6 Lennard-Jones (LJ) and Coulombic potentials, respectively. The Lorentz-Berthelot mixing rules[44, 45] were applied to determine the LJ parameters for unlike interactions from the parameters of the pure components. Distance cut-off for all non-bonded interactions was set to 1.4 nm. Long-range corrections to the electrostatic interactions were described using the particle mesh Ewald (PME) method with a Fourier grid spacing of 0.12 nm, a tolerance of 10^{-5}, and fourth-order interpolation. Periodic boundary conditions were applied in three dimensions for all simulations. We point out that in our systems AAs were present only on one side of the hydrate substrate. Because of periodic boundary conditions, the opposite side of the hydrate substrate remained exposed to the liquid organic phase. To ensure that differences in interfacial energy across the simulated hydrate substrate do not affect the results presented in this manuscript, we conducted additional simulations, for selected systems in which both sides of the hydrate substrate were covered by AAs, at the same surface density. Quantification of the results confirmed that the structure of the thin interfacial AAs layer, as well as the density profiles of methane along the Z direction of the simulation box with AAs on either one or both sides of the hydrate substrate are indistinguishable from each other (see Figures S5 and S6 of the SM).

Table 1. Compositions of the 17 simulated systems. Each system contains 696 methane molecules (432 within the hydrate structure and 264 dissolved in the hydrocarbon phase), 880 higher molecular weight alkanes (n-dodecane, n-octane, and n-hexane), and 2488 water molecules. At the highest surface density considered (0.89 molecules.nm^{-2}), 24 AA molecules are present at the hydrate-hydrocarbon interface.

Simulated system	**AAs type**	**Number of n-dodecane**	**Number of n-octane**	**Number of n-hexane**	**AAs surface density, molecules.nm^{-2}**
1	S_4L_8	880	-	-	0.22
2	S_4L_{12}				0.22
3	S_6L_{12}				0.22
4	S_4L_8	880	-	-	0.44
5	S_4L_{12}				0.44
6	S_6L_{12}				0.44
7	S_4L_8	880	-	-	0.67
8	S_4L_{12}				0.67
9	S_6L_{12}				0.67
10	S_4L_8	880	-	-	0.89
11	S_4L_{12}				0.89
12	S_6L_{12}				0.89
13	S_8L_{12}	880	-	-	0.89
14	S_4L_{12}	440	440	-	0.89
15	S_4L_{12}	-	880	-	0.89
16	S_4L_{12}	-	-	880	0.89
17	S_4L_8	-	880	-	0.89

EXPERIMENTAL DETAILS

The rocking cell apparatus was used to test the performance of selected AAs. A schematic for the apparatus and a close up picture of the rocking cells rig is provided in **Figure 3**.

The system used to test low-dosage hydrate inhibitors (LDHIs) consists of six-cell units. Each rocking cell consists in a Hastelloy cylindrical vessel of length ~ 11.37 cm and diameter ~ 1.85 cm, featuring dual sapphire windows and a powerful LED lighting system that allows for the clear observation of the testing fluids as the experiment is conducted. Each rocking cell can sustain pressures as high as 20 MPa in the T range from -10 to +70°C. The higher pressures and lower temperatures that can be sampled are consistent with those at which hydrates can form. The temperature is maintained at the desired level via a liquid bath, whose temperature can be controlled within ±0.1°C using an automatic controller. The pressure in the rocking cell is set initially by a dual piston pump (gas booster in Figure 3). The pressure is accurate to within 0.01 MPa at the beginning of the experiment. When the temperature decreases, the pressure also decreases, as expected based on classic thermodynamics. When the hydrates form, the pressure decreases because the gas is entrapped by the hydrates. One magnetic sphere is placed in each cell to provide agitation. Each cell houses two magnetic proximity sensors that detect and record any obstruction in the movement of the magnetic sphere. The formation of hydrates is detected when the pressure decreases abruptly within the cell. After hydrates formation, their agglomeration is detected by the slowing down, and/or the eventual stop of the magnetic sphere movement.

The system can be programmatically controlled (see **Figure 3**) to set temperatures, temperature ramp rates, rocking rates, and rocking angles. To mimic flow-assurance applications, both shut-in and restart scenarios can be simulated. For example, interrupting the rocking of the cell while maintaining the temperature constant simulates the shut-in scenario. From this condition, initiating the rocking of the cells simulates restart.

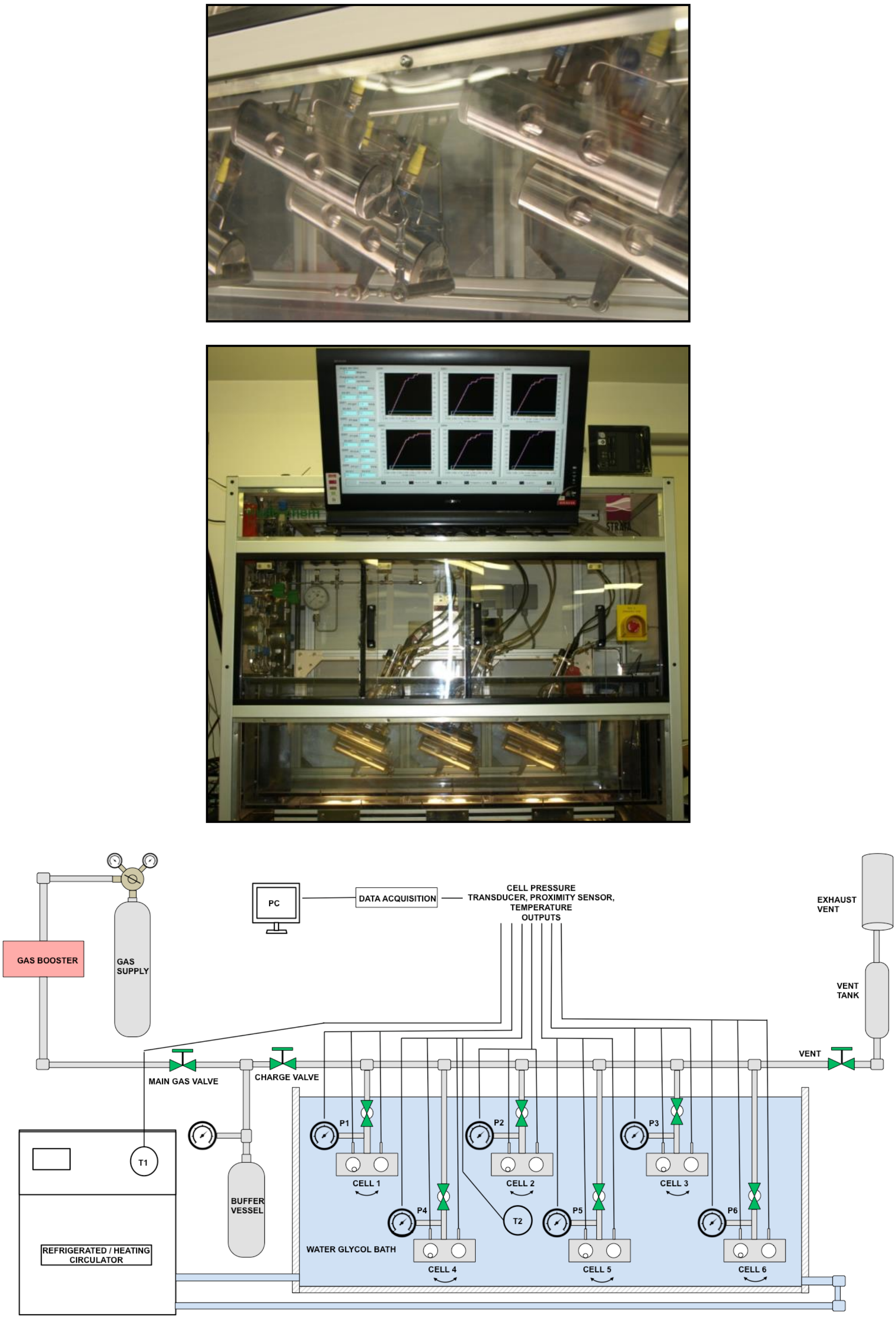

Figure 3. Close up of a six-unit rocking cell rig (top) and rocking cell rigs used for low-dosage hydrate inhibitor testing (middle). In the bottom panel we report a schematic diagram for the rocking cell rig.

The proper amount of oil, water and inhibitor were injected into the cells. Thereafter, the cells were pressurized to 13.8 MPa with Green Canyon gas, a common Gulf of Mexico Type II hydrate former. Green Canyon gas contains major components including methane (87.26 mol%), ethane (7.57 mol%), and propane (3.1 mol%) and minor amount of nitrogen (0.39 mol%) and other gases (0.49 mol% isobutene, 0.79 mol% n-butane, 0.2 mol% isopentane, and 0.2 mol% n-pentane). In the experiments, the liquid hydrocarbon phase is composed of dodecane. The water phase consisted of 3.5 wt% NaCl brine, as these are the conditions typically experienced upon sea water breakthrough during production. AAs were dosed into the cells at 2 vol% of the water volume. To compare across different molecules, the concentration of the actives in each AA was constant.

After pressurizing the cells to 13.8 MPa, an oil saturation period of 2 hours was followed by a cool-down period of 2 hours where the temperature was ramped down from 20 °C to 4 °C. After reaching the designated temperature, the cells were rocked for 16 to 18 hours and shut-in in the horizontal position for 6 hours. The cells were then restarted for 0.5 hour, and particular attention was paid to the critical restart period. Finally, the cells were warmed back to 20 °C while rocking. This test was conducted to simulate steady state as well as transient conditions in the field.

The experiments are conducted at various gas-oil-water ratios. Given the gas composition used in the experiments, it is expected that SII hydrates will form. Note that while the experiments were conducted at increasing water content, the simulations were conducted with no free water present in the system, other than a thin molecular layer formed on top of the hydrates. The AAs shown in **Figure 2** were used in the experiments reported herein.

RESULTS

Visual observation of simulation snapshots

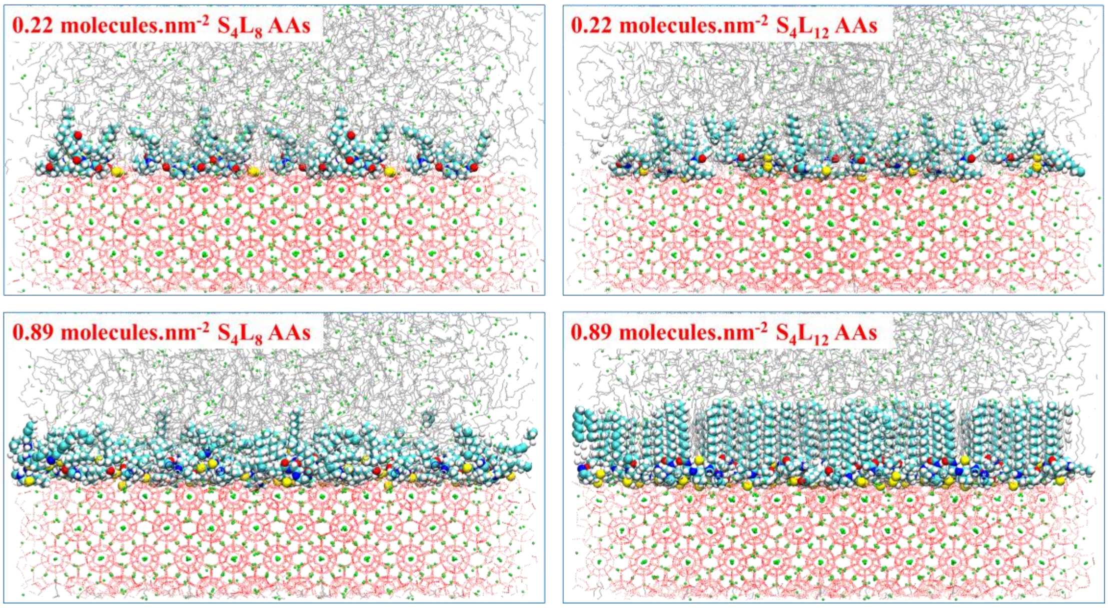

Figure 4. Representative simulation snapshots for systems containing S_4L_{12} (left panels) and S_4L_8 AAs (right panels) at two surface densities: 0.22 (top) and 0.89 molecules.nm^{-2} (bottom). Methane: green spheres; n-dodecane: silver lines; water connected by hydrogen bonds: red lines; chloride ions: yellow spheres; AAs: hydrogen, carbon, oxygen and nitrogen atoms are represented by white, cyan, red, and blue spheres, respectively.

Representative simulation snapshots of S_4L_8 and S_4L_{12} AAs adsorbed on the hydrate surface are shown in **Figure 4** at low (0.22 molecules.nm^{-2}) and high (0.89 molecules.nm^{-2}) surface densities. The snapshots are taken at the end of our simulations. For clarity, we replicate the simulation box twice in the X and Y directions. We observe that the head groups of AAs adsorb on the hydrate surface, possibly because of the strong attractive interactions between the polar functional groups of AAs and water molecules in the hydrate layer. The long tails of AAs are instead more likely to extend towards the alkane bulk phase, presumably because of the hydrophobicity of the alkyl tails. The snapshots shown in **Figure 4** suggest that different AAs yield different thin-film structures as the surface density increases. At low surface densities, the AAs hydrophobic tails do not show preferred orientation, irrespectively of the tail length. However, at sufficiently high surface densities, a pronounced difference is observed in the structure of the interfacial film depending upon molecular structure of AAs. Explicitly, S_4L_{12} AAs yield a very ordered thin film, within which the long tails of AAs and n-dodecane align parallel to each other in a nearly all-*trans* conformation (illustrated in **Figure S7** of the Supplemental Material (SM)) and orient perpendicularly to the hydrate surface. This ordered structure was not observed when using S_4L_8, even at high surface density. As discussed below, it is possible that our results for S_4L_{12} are consistent with an interfacial-freezing phenomenon.

Density profiles

In order to quantify the influence of AAs adsorbed on the hydrate surface on the distribution of methane and n-dodecane in the system, we calculated atomic density profiles along the Z direction of the simulation box.

Atomic density profiles of total carbon atoms calculated for systems containing either S_4L_8 or S_4L_{12} AAs at various surface densities are reported in **Figure S8** of the SM. It can be seen from that figure that at higher S_4L_{12} surface densities (0.67 and 0.89 molecules.nm^{-2}), the thin interfacial AAs layer is highly packed. It could be because the AAs long tails and dodecane molecules formed a well-ordered layer near the hydrate surface resembling a "solid-like" structure, as will be discussed below. We report in **Figure 5** density profiles for methane. These results show periodic peaks from Z = 0 to ~ 3.2 nm. These peaks are due to the methane molecules trapped in the hydrate cages. At Z > 5 or 6 nm, depending on the system, the results show a uniform density because the hydrocarbon phase is fluid. At the hydrate-fluid interface methane comes from both the hydrate and the fluid phase. Because it is possible that free methane molecules accumulate in this region towards growing the hydrate, the density profiles in this region is typically larger than that found in the fluid phase. The results discussed so far do not depend strongly on the AAs type nor surface density. On the contrary, the methane density profile in the thin region between the layer of AAs head groups and the bulk liquid hydrocarbon phase shows pronounced dependency on AAs type. At low AAs surface densities, the density of methane near the hydrate surface for systems containing either S_4L_8 or S_4L_{12} are similar to those found in the bulk. When S_4L_8 is considered, the results show a depletion of methane at the interface as the AAs surface density increases to 0.89 molecules.nm^{-2}, but overall the changes are minimal. On the contrary, when S_4L_{12} is considered, the depletion of methane is very pronounced and the density profiles in the interfacial region are nearly 0 when the AAs surface density reaches 0.67 molecules.nm^{-2}. Combined with visual observation of the simulation snapshots, these results suggest that the ordered layer of S_4L_{12} tails successfully expels methane from the interfacial region. This phenomenon seems to be due to the formation of an ordered film with AAs tails and n-dodecane molecules synergistically expelling methane.

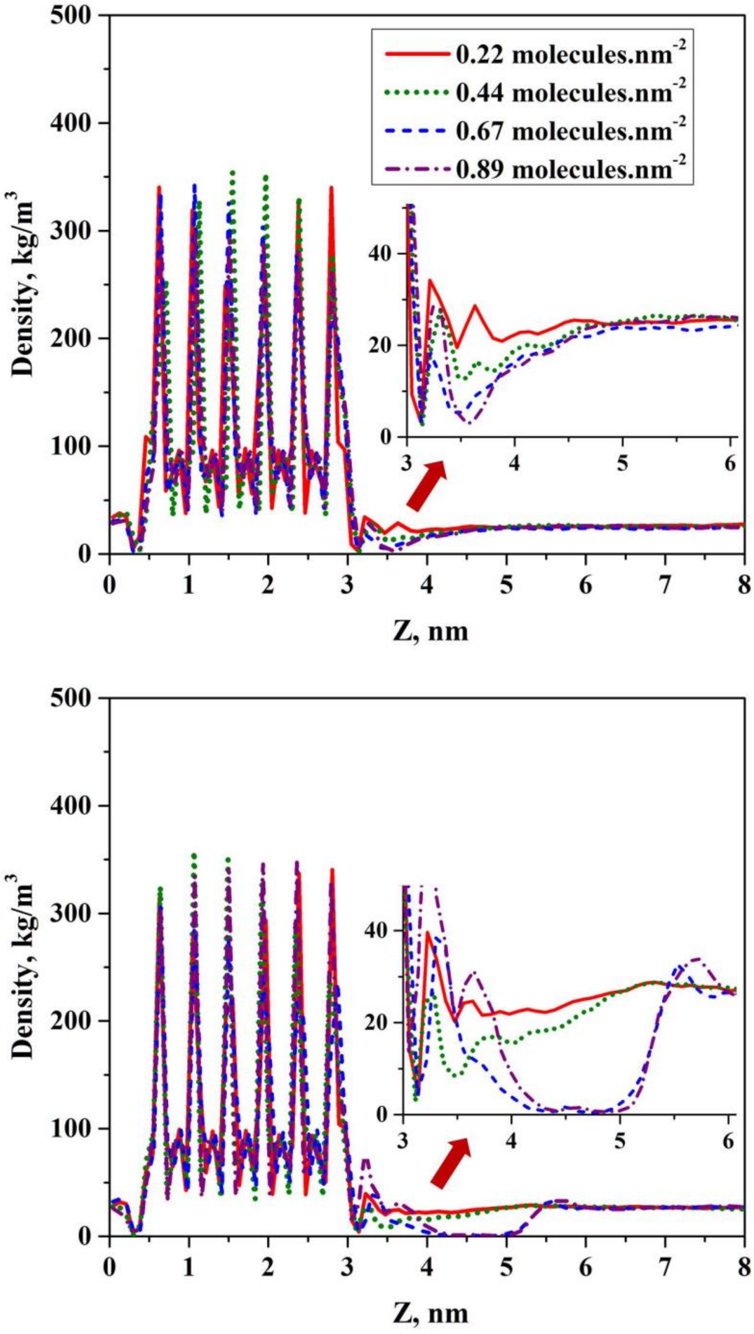

Figure 5. Density profiles of methane along the Z direction of the simulation box for systems with S_4L_8 (top) and S_4L_{12} AAs (bottom). Different curves are obtained at increasing AAs surface densities: 0.22 (red solid line), 0.44 (green dot line), 0.67 (blue dash line), and 0.89 (purple dash dot line) molecules.nm^{-2}.

AAs orientation and molecular extension

To quantify the orientation of the AAs at the interface, we considered the angle formed between each tail and the direction perpendicular to the hydrate surface. We calculated the probability distribution of this angle (which we call 'orientational angle', ϕ), as well as that of the angle between the two long tails of one AA molecule (which we call ‘conformational angle’, θ). See the top panel of **Figure 6** for a schematic of both angles.

In **Figure 6,** we report the probability distribution of the orientational angle in the middle panels, and that of the conformational angle in the bottom panels. We consider S_4L_8 and S_4L_{12} AAs (left and right panels, respectively) at various surface densities. At low surface densities, 0.22 and 0.44 molecules.nm^{-2}, the orientational angle shows wide probability distributions, from 0° to 90° and above, irrespectively of the AA tail length. Similarly, the conformational angle does not show preferential values at low surface coverage for either AAs considered. These results suggest that the AAs are rather disordered at these conditions. However, when the AAs surface density increases, the results show significant variations. While the results obtained for S_4L_8 AAs do not show substantial changes compared to those obtained at low surface density, the results obtained for S_4L_{12} AAs show pronounced order. The orientational distributions show pronounced peaks at ~ 20° and ~10° when the surface density increases to 0.67 and 0.89 molecules.nm^{-2}, respectively, suggesting that the AAs tails become almost perpendicular to the hydrate surface. At the same surface densities, the conformational distributions show pronounced peaks at ~ 10°, suggesting that the AAs maintain their long tails almost parallel to each other at these conditions.

As the only difference between the systems simulated is the length of the AAs tails, the differences highlighted in **Figure 4**, **Figure 5**, and **Figure 6** are likely due to steric effects (the longer tails pack more efficiently when perpendicular to the interface), interactions with the underlying hydrate (the shorter tails should experience weaker effective repulsions than the longer ones), and perhaps also preferential interactions with the hydrocarbon molecules in the fluid phase (the short tails are less compatible than the long ones with the n-dodecane molecules).

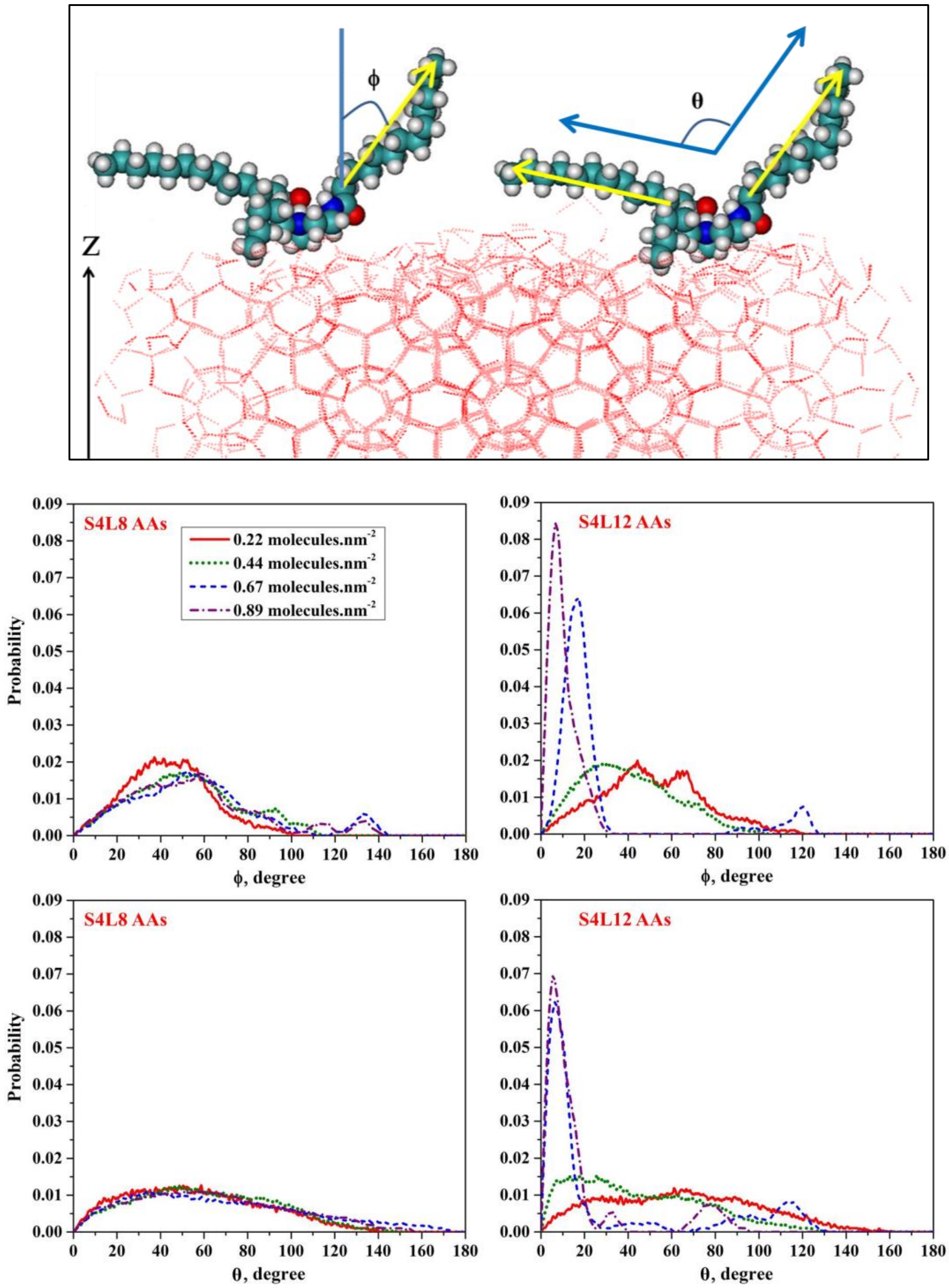

Figure 6. Top panel: schematic representing the orientational angle ϕ (angle formed by the vector connecting the first-the last carbon of the hydrocarbon tails and the surface normal (the Z direction) (left), and the conformational angle θ between two long tails of one AA molecule (right). Middle and bottom panels: probability distributions of orientational and conformational angles, for S_4L_8 and S_4L_{12} AAs (left and right panels, respectively) at increasing AAs surface density: 0.22 (red solid line), 0.44 (green dot line), 0.67 (blue dash line) and 0.89 (purple dash dot line) molecules.nm^{-2}.

We point out that when the ordered film described for S_4L_{12} AAs forms at the hydrate-hydrocarbon interface, visual inspection of simulation snapshots suggests that n-dodecane molecules from the liquid phase penetrate the AAs layer and remain approximately parallel to the AAs tails and perpendicular to the solid substrate (see **Figure 4** and SM).

It is possible that the AA long tails and alkane in AA layer are in fully extended conformations. In **Figure 7**, we plot the length of either S_4L_8 or S_4L_{12} AAs long tails (left panel) and that of n-dodecane molecules found within the thin film formed by AAs on the hydrates (right panel) at various AAs surface densities. In this analysis, the chain length is represented by the end-to-end distance between the first and the last carbon atoms of the chain. N-dodecane molecules are considered within the thin AAs film when their center of mass is within the region between the AAs head groups and the out most CH_3- groups of AAs alkyl tails (see **Figure S9** of the SM). When S_4L_8 AAs are considered, the chain length of both AAs tails and n-dodecane molecules is independent from the surface density. The values remain constant at ~0.82 nm and 1.2 nm, respectively. Note that the end-to-end length of n-dodecane in the bulk is ~1.18 nm. On the contrary, when S_4L_{12} AAs is considered, as the AAs surface density increases, our results suggest that there is a tendency of AAs long tails and n-dodecane to extend further. The length of AAs long tails and n-dodecane in the thin AAs film at high surface densities is ~ 1.36 – 1.4 nm, close to the length of n-dodecyl in the all-*trans* conformation, ~ 1.5 – 1.6 nm.[46-48] Combined with visual observation of simulation snapshots (see **Figure S7** of the SM), these results suggest that within the ordered film of AAs the long alkyl tails of S_4L_{12} AAs and n-dodecane are extended to reach the all-*trans* conformation, which allows for more attractive chain-chain lateral van der Waals interactions.

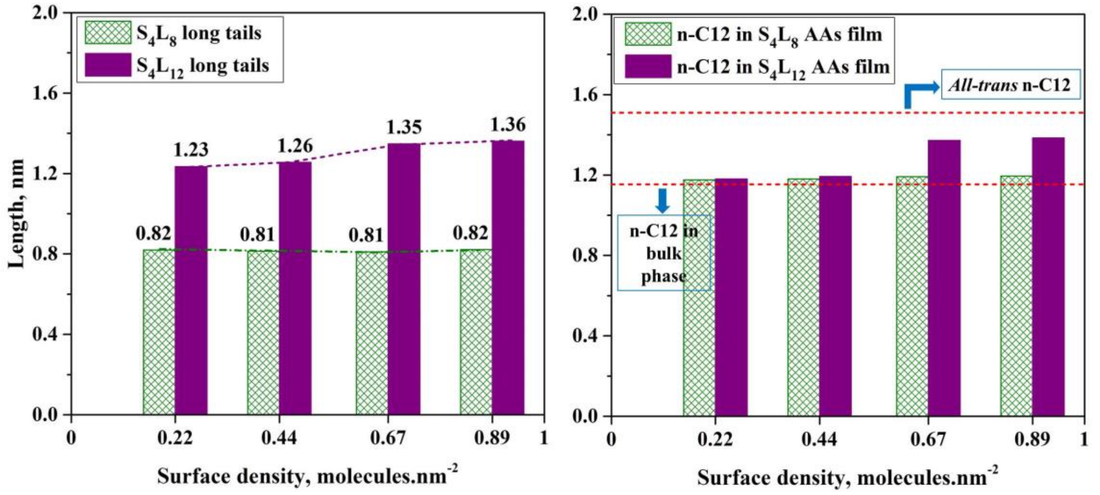

Figure 7. Left panel: alkyl tail length of S_4L_8 (green fence) and S_4L_{12} AAs (purple solid) at different surface densities. Right panel: n-dodecane chain length in the thin film of S_4L_8 (green fence), and S_4L_{12} AAs (purple solid) at different AAs surface densities.

Rocking Cell Experimental Performance

AAs typically perform well when the amount of water present in the system is low, and the hydrates plug form readily when the amount of water increases. It is customary to refer to the amount of water present in terms of 'water cut', which is the volume of water with respect to the volume of liquid in the system. For a given water cut, the best performing AAs would prevent hydrates agglomeration at low concentrations. Based on these observations, in our experiments we determined the primary performance criteria for AAs by the maximum water cut an AA can treat. For one AA, a series of rocking cell tests were run to determine the performance limits of each AA molecule (see **Figure 2** for structure), starting from low water cut and increasing the water cut while keeping the AA concentration in water constant. The lowest water cut considered was 25 vol% and the typical AA concentration in the experiments was of 2 vol% in water. The highest water cut at which some of the AAs considered prevented the formation of hydrates in the systems considered here was of 55 vol%. The experiments were performed following the protocol described in Experimental Details.

Table 2 provides a summary of the experimental data obtained from rocking cell testing. The experiments summarize, qualitatively, visual observation: the AAs are classified as good, moderate or poor performers based on the maximum water cut at which the AA is effective at preventing hydrates from plugging the rocking cells. In our analysis, ‘good’ performance indicates that the AA was able to prevent the formation of hydrates at water cuts greater or equal than 50 vol%; ‘moderate’ is 30-45% and ‘poor’ less than 30%. While the results are semi-quantitative, they are important for identifying the AAs that are expected to perform well in practical applications.

Table 2. Performance assessment of different AA molecules.

R1	**R2**	**Notation**	**Performance Category**
C12	C4	S_4L_{12}	Good
C12	C5	S_5L_{12}	Moderate
C12	C6	S_6L_{12}	Poor
C12	C8	S_8L_{12}	Poor
C8	C4	S_4L_8	Poor

DISCUSSION

Our results suggest that an ordered AAs film at the interface between a hydrate and a fluid liquid hydrocarbon phase can be effective at excluding methane from the interfacial layer. It is possible that the depletion of methane from the interface impedes hydrate growth, one of the mechanisms to control during flow assurance problems (the others include hydrate nucleation and aggregation). It is perhaps interesting to observe that, out of the two AAs simulated above, the one that shows better performance in practical applications is S_4L_{12}, which in our simulations yields an ordered film that excludes methane from the interface. Analysis of density profiles reveals that the ordered AAs film is highly packed with oil molecules aligned parallel to the AAs long tails. Based on this observation, we also suggest that the formation of an ordered thin AAs film on the hydrate surface could yield a barrier preventing the aggregation of water droplets or hydrate particles on the underlying hydrate. We expect that a low-density disordered AAs layer would not be able to provide such a barrier. We are conducting free energy calculations to quantify such phenomena. It should be however pointed out that in the experiments the better performing AAs are those that are effective as the water content increases, while in the simulations there is no free water present, other than a thin molecular film that form spontaneously on the hydrate surface. Future studies are planned to quantify the effect of water on the simulation results.

The ordered film described above for S_4L_{12} AAs at the interface between hydrates and liquid hydrocarbons consisting primarily of n-dodecane seems consistent with the 'interfacial-freezing' phenomenon. This phenomenon has been documented for water-alkane or air-alkane interfaces in the presence of cation surfactants.[49-51] Tamam et al.[49] used X-ray reflectivity and surface tensiometry to study the surfactants at the oil-water interface; at high temperatures the results were consistent with a liquid interfacial monolayer formed by surfactant tails and alkane molecules at the interface. As the temperature decreases, the results showed that the interfacial layer becomes dense and frozen, with alkane molecules and surfactant tail in fully extended state even at temperatures well above the alkane freezing temperature. It has been proposed that a reduction in partial molar entropy induced by strong van der Waals interactions between alkane molecules incorporated in the surfactant film and the surfactants tails is responsible for this phenomenon.[51] For completeness, we point out that the formation of ordered AAs films strongly depends on thermodynamic conditions. For example, additional simulations, not reported here for brevity, show that the ordered film observed for S_4L_{12} AAs at 0.67 molecules.nm^{-2} becomes disordered when the temperature is increased to 290 K, all other parameters being constant.

To examine the structure of the thin interfacial film formed by AAs and n-dodecane, in-plane radial distribution functions (RDFs) were calculated among the n-dodecane molecules within the AAs film. We used the position of the 6th carbon atom in the n-dodecane chain for these calculations. The results are shown in **Figure 8**.

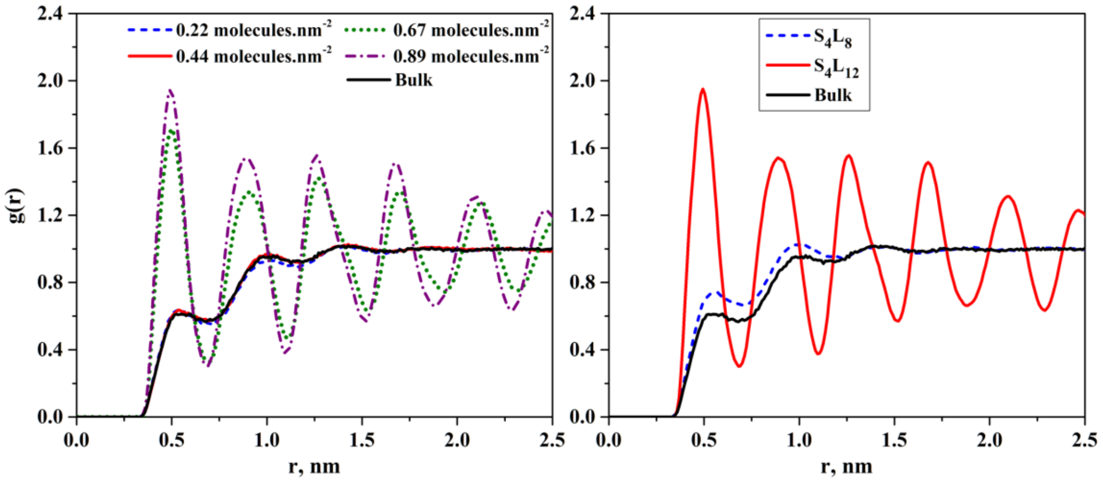

Figure 8. Left panel: in-plane radial distribution functions between n-dodecane molecules in the bulk liquid phase (black solid line) and at the interfacial layer at different S_4L_{12} AAs surface densities: 0.22 (blue dash line), 0.44 (red solid line), 0.67 (green dot line), and 0.89 molecules.nm^{-2} (purple dash dot line). Right panel: in-plane radial distribution functions between n-dodecane molecules in bulk liquid phase (black solid line), and within the interfacial film formed by S_4L_8 (blue dash line) or by S_4L_{12} AAs (red solid line) at the surface density of 0.89 molecules.nm^{-2}.

In **Figure 8,** we compare the RDF obtained for n-dodecane in the bulk liquid hydrocarbon phase to RDFs obtained for the n-dodecane molecules found within the thin film formed by S_4L_{12} AAs on the hydrates. The bulk results are consistent with a fluid structure, as expected. Even when the n-dodecane molecules are found within the thin interfacial film, the RDFs are consistent with a fluid structure, unless the S_4L_{12} AAs surface density increases to 0.67 molecules.nm^{-2} and above. In the latter case the RDFs are indicative of an ordered structure. In the right panel of **Figure 8,** we compare the bulk RDF for n-dodecane to RDFs obtained for n-dodecane within the thin interfacial films in the presence of either S_4L_8 or S_4L_{12} AAs at 0.89 molecules.nm^{-2}. We conclude that n-dodecane remains fluid-like and disordered when S_4L_8 AAs are simulated. However, perhaps more importantly, these results are consistent with the formation of an apparently frozen interfacial layer in the presence of S_4L_{12} AAs at sufficiently high surface density. AAs with shorter tails do not yield such a dense and ordered film.

Because in our simulations the formation of the apparently frozen interfacial film was observed when the length of the AAs long tails was comparable to the length of the linear hydrocarbon present in the fluid mixture (n-dodecane) and not otherwise, it is possible that aside the surface AAs density, other factors influence the formation of the dense and ordered interfacial film, including lateral van der Waals interactions between the AA tails and alkane, compatibility between AA and alkane chain length, the ability of the AAs molecules to pack in an ordered structure, which may be affected by the molecular architecture of the head group and of the other tails, if present, as well as the smoothness of the hydrate substrate, and possibly other factors such as the presence of impurities etc. In what follows we quantify some of these effects.

Effect of the AAs molecular features: the short tail

We conducted different simulations using S_4L_{12}, S_6L_{12}, and S_8L_{12} AAs at the surface density of 0.89 molecules.nm^{-2}. We calculated the various properties discussed above, as they are considered signatures of the tendency of the AAs to form dense films. The quantities of interest are the probability distribution of the orientational angle, the RDF between n-dodecane molecules within the interfacial film, and the atomic density profiles in the Z direction (see **Figures S11** of the SM).

The results for the probability distribution of the orientational angle (top left panel in **Figure S11** of the SM) show that as the length of the short tail increases, the two long tails show a more dispersed orientation with respect to the surface normal. The results for the RDFs computed among n-dodecane molecules within the interfacial film (top right panel in **Figure S11** of the SM) show that as the short tail length increases the thin interfacial film remains ordered, but the peaks in the RDFs become broader and less pronounced. The results for the density profiles of methane in the direction perpendicular to the interface (bottom right panel in **Figure S11** of the SM) show that as the short tail of the AAs increases in length, methane penetrates the interfacial film. All the results just discussed consistently show that the order of the AAs film at the hydrate-hydrocarbon interface decreases as the length of the short tail in the AAs considered here increases.

To explain the effects due to the short tail length, we calculated the probability distribution of the orientational angle for the short tail. The results are shown in **Figure S12** of the SM, and suggest that as the tail increases in length it becomes more and more oriented perpendicularly to the hydrate surface. This suggests that when the third tail is too long, it competes with the other two tails for space within the interfacial layer, thus compromising the compactness of the film, allowing methane to penetrate the interfacial layer. It is also possible that as the third tail orients away from the interface the AA molecule adheres less strongly to the hydrate surface, although this possibility has not been tested herein.

Effect of the liquid hydrocarbon type

We assessed how the structure of the S_4L_{12} AAs film, surface density of 0.89 molecules.nm^{-2} on the hydrate, changes in the presence of n-octane or n-hexane rather than n-dodecane. The system conditions were not changed (T=277 K, P = 20 MPa). The results are analyzed in terms of the probability distribution of the orientational angle, density profiles of carbon atoms, methane along the Z direction, and RDFs between the hydrocarbons within the interfacial film (see **Figure S13** of the SM). The results clearly show that the AAs films obtained when the n-dodecane is substituted with either n-octane or n-hexane are much less ordered and are not capable to expel methane from the interfacial region.

From the results shown in **Figure S13** of the SM**,** it appears that the AAs S_4L_{12} yield an ordered and dense interfacial film when n-dodecane is present in the hydrocarbon fluid mixture. It is possible that when the length of the long tails in the AAs molecules is comparable to the length of the hydrocarbon chains in the fluid mixture, inter-digitation of the hydrocarbon molecules within the film formed by the AAs molecules yields higher partial molecular entropy compared to the systems containing hydrocarbon chains of different lengths, yielding the dense ordered film discussed above.

We also simulated S_4L_8 AAs at the surface density of 0.89 molecules.nm^{-2} when the hydrocarbon fluid contained n-octane solvent. The results, which can be found in **Figure S14** of the SM, show that the interfacial film remains disordered and not able to exclude methane from the interfacial region. It is possible that the relatively short length of the tails in S_4L_8 AAs prevents the formation of ordered interfacial films.

Finally, we simulated the system containing S_4L_{12} AAs at the surface density of 0.89 molecules.nm^{-2} at contact with a fluid hydrocarbon mixture that contained, in addition to methane, both n-octane and n-dodecane at the 1:1 molar ratio. The results (see **Figure S15** of the SM) are consistent with the formation of a dense ordered AAs films near the hydrate surface. Analysis of the simulation results shows that 93% of the hydrocarbon chains present within the interfacial AAs film were n-dodecane, suggesting a significant enrichment compared to the composition of the bulk hydrocarbon fluid. This result suggests that perhaps AAs whose tails are compatible with the hydrocarbons present in the liquid phase could be more effective in flow assurance applications. It should also be pointed out that the preferential adsorption of n-dodecane within the AAs film is consistent with the findings of Tokiwa et al.,[51] who reported a preferential adsorption of alkane molecules of length similar to that of surfactant tails into the surfactant layer at the oil-water interface upon freezing of the interface.

CONCLUSIONS

We conducted equilibrium molecular dynamics simulations at the atomistic resolution to investigate the behavior of anti-agglomerants adsorbed at the interface between one flat hydrate surface and a fluid hydrocarbon mixture containing methane and higher molecular weight hydrocarbons. The anti agglomerants used in this study were chosen because they offer the possibility to systematically vary the length of their hydrophobic tails. The effect of these changes was analyzed both via simulations and experiments conducted with the rocking cell apparatus. The molecules contain amide and tertiary ammonium cation groups in their head groups and have three tails of varying lengths. In the simulations the length of the anti-agglomerant tails and the anti agglomerants surface density were changed systematically. Analysis of the simulation results and comparison against experimental data reveal that those anti-agglomerants that show better practical performance can yield dense ordered films at the hydrate-hydrocarbon interface, from which methane molecules are excluded. This dense ordered layer is consistent with the ‘frozen interfacial layers’ reported for several water-oil interfaces in the presence of surfactants. A number of parameters, including surface density of the anti-agglomerants, their molecular structure, capability to pack in an ordered ensemble, preferential interactions with both the underlying hydrate substrate and the supernatant hydrocarbon phase, as well as the presence of impurities seem to be able to affect the structure of this interfacial film, and therefore its ability to exclude methane from the interfacial region. Should these results be verified experimentally, they could lead to a better understanding of the molecular mechanisms by which anti-agglomerants can be effective in the management of hydrates formation and agglomeration in flow assurance problems, and perhaps also for developing new technologies to both harvest natural gas hydrates and engineer carbon dioxide hydrates for long-term storage applications.

Associated Content:

Supplemental Material.

Algorithms implemented for density profile calculation; distribution of F4 order parameter for water across the hydrate substrate; evaluation of simulation equilibration and the effect of AAs on both sides of the hydrate layer; simulation snapshots for (1) n-dodecane molecules within the S_4L_{12} AAs layer at different surface densities (0.44 and 0.89 molecules.nm^{-2}) and (2) systems with different AAs and different types of alkanes; results for (1) density profiles of AAs, methane and all carbon atoms along the Z direction of the simulation, (2) probability distributions of orientational angle of AAs, and (3) in-plane radial distribution functions between long-chain alkane molecules (hexane, octane, dodecane) in the bulk liquid phase and at the interfacial layer. The Supplemental Material is available free of charge via the Internet at http://pubs.acs.org.

ACKNOWLEDGEMENTS

We would like to thank financial support provided by Halliburton, the UK Engineering, and Physical Sciences Research Council (EPSRC) under grant number EP/N007123/1. Generous allocations of computing time were provided by the University College London Research Computing Platforms Support (LEGION), and the National Energy Research Scientific Computing Center (NERSC) at Lawrence Berkeley National Laboratory.

REFERENCES

(1) Sloan, E. D.; Koh, C.; Sum, A. K.; Ballard, A. L.; Creek, J.; Eaton, M.; Lachance, J.; McMullen, N.; Palermo, T.; Shoup, G.; Talley, L. *Natural Gas Hydrates in Flow Assurance*; Gulf Professional Pub./Elsevier: Boston, 2011. p 1-200.

(2) Rochelle, C. A.; Camps, A. P.; Long, D.; Milodowski, A.; Bateman, K.; Gunn, D.; Jackson, P.; Lovell, M. A.; Rees, J. Can CO2 hydrate assist in the underground storage of carbon dioxide? *Geological Society, London, Special Publications*, **2009,** *319* (1), 171-183.

(3) Majorowicz, J.; Grasby, S. E.; Safanda, J.; Beauchamp, B. Gas hydrate contribution to Late Permian global warming. *Earth and Planetary Science Letters*, **2014,** *393*, 243-253.

(4) Kvenvolden, K. A. Potential effects of gas hydrate on human welfare. *Proceedings of the National Academy of Sciences of the United States of America*, **1999,** *96* (7), 3420-3426.

(5) Sloan, E. D.; Koh, C. A. *Clathrate Hydrates of Natural Gases, Third Edition*; Crc Press-Taylor & Francis Group: Boca Raton, 2008; Vol. 119. p 1-701.

(6) Bollavaram, P. Hydrate plug dissociation in pipelines by pressure reduction: Experiment and modeling. Doctor of Philosophy, Colorado School of Mines2002.

(7) Stewart Jr, M. I. Chapter Five - Hydrate Prediction and Prevention. In *Surface Production Operations (Third Edition)*, Stewart, M. I., Ed.; Gulf Professional Publishing: Boston, 2014; Vol. 2, pp 215-258.

(8) Koh, C. A.; Westacott, R. E.; Zhang, W.; Hirachand, K.; Creek, J. L.; Soper, A. K. Mechanisms of gas hydrate formation and inhibition. *Fluid Phase Equilibria*, **2002,** *194–197*, 143-151.

(9) Kelland, M. A. History of the Development of Low Dosage Hydrate Inhibitors. *Energy & Fuels*, **2006,** *20* (3), 825-847.

(10) Sloan, E. D. Method for controlling clathrate hydrates in fluid systems. US Patents US5880319 A, 1995.

(11) Lederhos, J. P.; Long, J. P.; Sum, A.; Christiansen, R. L.; Sloan Jr, E. D. Effective kinetic inhibitors for natural gas hydrates. *Chemical Engineering Science*, **1996,** *51* (8), 1221-1229.

(12) Kelland, M. A.; Svartaas, T. M.; Øvsthus, J.; Tomita, T.; Mizuta, K. Studies on some alkylamide surfactant gas hydrate anti-agglomerants. *Chemical Engineering Science*, **2006,** *61* (13), 4290-4298.

(13) Kelland, M. A.; Svartås, T. M.; Andersen, L. D. Gas hydrate anti-agglomerant properties of polypropoxylates and some other demulsifiers. *Journal of Petroleum Science and Engineering*, **2009,** *64* (1–4), 1-10.

(14) Klomp, U. C.; Kruka, V. R.; Reijnhart, R.; Weisenborn, A. J. Method for inhibiting the plugging of conduits by gas hydrates. US Patents US5648575 A, 1997.

(15) Aman, Z. M.; Sloan, E. D.; Sum, A. K.; Koh, C. A. Adhesion force interactions between cyclopentane hydrate and physically and chemically modified surfaces. *Physical Chemistry Chemical Physics*, **2014,** *16* (45), 25121-25128.

(16) de Boer, M. P.; de Boer, P. C. T. Thermodynamics of capillary adhesion between rough surfaces. *Journal of Colloid and Interface Science*, **2007,** *311* (1), 171-185.

(17) Phan, A.; Bui, T.; Acosta, E.; Krishnamurthy, P.; Striolo, A. Molecular mechanisms responsible for hydrate anti-agglomerant performance. *Physical Chemistry Chemical Physics*, **2016,** *18* (36), 24859-24871.

(18) Huo, Z.; Freer, E.; Lamar, M.; Sannigrahi, B.; Knauss, D. M.; Sloan Jr, E. D. Hydrate plug prevention by anti-agglomeration. *Chemical Engineering Science*, **2001,** *56* (17), 4979-4991.

(19) Makogon TY, S. E. In *Mechanism of kinetic hydrate inhibitors* The 4th International Conference on Gas Hydrates, Yokohama, Japan, 2002.

(20) Kelland, M. A.; Svartaas, T. M.; Øvsthus, J.; Tomita, T.; Chosa, J.-i. Studies on some zwitterionic surfactant gas hydrate anti-agglomerants. *Chemical Engineering Science*, **2006,** *61* (12), 4048-4059.

(21) Eastoe, J. Surfactant Aggregation and Adsorption at Interfaces. In *Colloid Science*; Blackwell Publishing Ltd., 2009, pp 50-76.

(22) Pisárčik, M.; Rosen, M. J.; Polakovičová, M.; Devínsky, F.; Lacko, I. Area per surfactant molecule values of gemini surfactants at the liquid–hydrophobic solid interface. *Journal of Colloid and Interface Science*, **2005,** *289* (2), 560-565.

(23) Hess, B.; Kutzner, C.; van der Spoel, D.; Lindahl, E. GROMACS 4: Algorithms for Highly Efficient, Load-Balanced, and Scalable Molecular Simulation. *Journal of Chemical Theory and Computation*, **2008,** *4* (3), 435-447.

(24) Van Der Spoel, D.; Lindahl, E.; Hess, B.; Groenhof, G.; Mark, A. E.; Berendsen, H. J. C. GROMACS: Fast, flexible, and free. *Journal of Computational Chemistry*, **2005,** *26* (16), 1701-1718.

(25) Takeuchi, F.; Hiratsuka, M.; Ohmura, R.; Alavi, S.; Sum, A. K.; Yasuoka, K. Water proton configurations in structures I, II, and H clathrate hydrate unit cells. *J Chem Phys*, **2013,** *138* (12), 124504.

(26) Chou, I.-M.; Sharma, A.; Burruss, R. C.; Shu, J.; Mao, H.-k.; Hemley, R. J.; Goncharov, A. F.; Stern, L. A.; Kirby, S. H. Transformations in methane hydrates. *Proceedings of the National Academy of Sciences*, **2000,** *97* (25), 13484-13487.

(27) Shu, J.; Chen, X.; Chou, I. M.; Yang, W.; Hu, J.; Hemley, R. J.; Mao, H.-k. Structural stability of methane hydrate at high pressures. *Geoscience Frontiers*, **2011,** *2* (1), 93-100.

(28) Schicks, J. M.; Ripmeester, J. A. The Coexistence of Two Different Methane Hydrate Phases under Moderate Pressure and Temperature Conditions: Kinetic versus Thermodynamic Products. *Angewandte Chemie International Edition*, **2004,** *43* (25), 3310-3313.

(29) Staykova, D. K.; Kuhs, W. F.; Salamatin, A. N.; Hansen, T. Formation of Porous Gas Hydrates from Ice Powders: Diffraction Experiments and Multistage Model. *The Journal of Physical Chemistry B*, **2003,** *107* (37), 10299-10311.

(30) Fleyfel, F.; Devlin, J. P. Carbon dioxide clathrate hydrate epitaxial growth: spectroscopic evidence for formation of the simple type-II carbon dioxide hydrate. *The Journal of Physical Chemistry*, **1991,** *95* (9), 3811-3815.

(31) Walsh, M. R.; Koh, C. A.; Sloan, E. D.; Sum, A. K.; Wu, D. T. Microsecond Simulations of Spontaneous Methane Hydrate Nucleation and Growth. *Science*, **2009,** *326* (5956), 1095-1098.

(32) Vatamanu, J.; Kusalik, P. G. Heterogeneous Crystal Growth of Methane Hydrate on Its sII [001] Crystallographic Face. *The Journal of Physical Chemistry B*, **2008,** *112* (8), 2399-2404.

(33) Anderson, B. J.; Tester, J. W.; Borghi, G. P.; Trout, B. L. Properties of Inhibitors of Methane Hydrate Formation via Molecular Dynamics Simulations. *Journal of the American Chemical Society*, **2005,** *127* (50), 17852-17862.

(34) Kvenvolden, K. A. Gas hydrates—geological perspective and global change. *Reviews of Geophysics*, **1993,** *31* (2), 173-187.

(35) Pronk, S.; Páll, S.; Schulz, R.; Larsson, P.; Bjelkmar, P.; Apostolov, R.; Shirts, M. R.; Smith, J. C.; Kasson, P. M.; van der Spoel, D.; Hess, B.; Lindahl, E. GROMACS 4.5: a high-throughput and highly parallel open source molecular simulation toolkit. *Bioinformatics*, **2013,** *29* (7), 845-854.

(36) Abascal, J. L. F.; Sanz, E.; García Fernández, R.; Vega, C. A potential model for the study of ices and amorphous water: TIP4P/Ice. *The Journal of Chemical Physics*, **2005,** *122* (23), 234511.

(37) Conde, M. M.; Vega, C. Determining the three-phase coexistence line in methane hydrates using computer simulations. *The Journal of Chemical Physics*, **2010,** *133* (6), 064507.

(38) Jensen, L.; Thomsen, K.; von Solms, N.; Wierzchowski, S.; Walsh, M. R.; Koh, C. A.; Sloan, E. D.; Wu, D. T.; Sum, A. K. Calculation of Liquid Water−Hydrate−Methane Vapor Phase Equilibria from Molecular Simulations. *The Journal of Physical Chemistry B*, **2010,** *114* (17), 5775-5782.

(39) Alireza Bagherzadeh, S.; Alavi, S.; Ripmeester, J. A.; Englezos, P. Why ice-binding type I antifreeze protein acts as a gas hydrate crystal inhibitor. *Physical Chemistry Chemical Physics*, **2015,** *17* (15), 9984-9990.

(40) Martin, M. G.; Siepmann, J. I. Transferable Potentials for Phase Equilibria. 1. United-Atom Description of n-Alkanes. *The Journal of Physical Chemistry B*, **1998,** *102* (14), 2569-2577.

(41) Wang, J.; Wolf, R. M.; Caldwell, J. W.; Kollman, P. A.; Case, D. A. Development and testing of a general amber force field. *Journal of Computational Chemistry*, **2004,** *25* (9), 1157-1174.

(42) D.A. Case, V. B., J.T. Berryman, R.M. Betz, Q. Cai, D.S. Cerutti, T.E. Cheatham, III, T.A. Darden, R.E. Duke, H. Gohlke, A.W. Goetz, S. Gusarov, N. Homeyer, P. Janowski, J. Kaus, I. Kolossváry, A. Kovalenko, T.S. Lee, S. LeGrand, T. Luchko, R. Luo, B. Madej, K.M. Merz, F. Paesani, D.R. Roe, A. Roitberg, C. Sagui, R. Salomon-Ferrer, G. Seabra, C.L. Simmerling, W. Smith, J. Swails, R.C. Walker, J. Wang, R.M. Wolf, X. Wu and P.A. Kollman. *AMBER 14*, University of California, San Francisco, 2014.

(43) Smith, D. E.; Dang, L. X. Computer simulations of NaCl association in polarizable water. *The Journal of Chemical Physics*, **1994,** *100* (5), 3757-3766.

(44) Lorentz, H. A. Ueber die Anwendung des Satzes vom Virial in der kinetischen Theorie der Gase. *Annalen der Physik*, **1881,** *248* (1), 127-136.

(45) Berthelot, D. Sur le mélange des gaz. *Compt. Rendus*, **1898,** *126*, 1703-1706.

(46) Schrettl, S.; Stefaniu, C.; Schwieger, C.; Pasche, G.; Oveisi, E.; Fontana, Y.; Morral, A. F. i.; Reguera, J.; Petraglia, R.; Corminboeuf, C.; Brezesinski, G.; Frauenrath, H. Functional carbon nanosheets prepared from hexayne amphiphile monolayers at room temperature. *Nat Chem*, **2014,** *6* (6), 468-476.

(47) Burgess, I.; Zamlynny, V.; Szymanski, G.; Lipkowski, J.; Majewski, J.; Smith, G.; Satija, S.; Ivkov, R. Electrochemical and Neutron Reflectivity Characterization of Dodecyl Sulfate Adsorption and Aggregation at the Gold−Water Interface. *Langmuir*, **2001,** *17* (11), 3355-3367.

(48) Vögtle, F.; Ballauf, M. *Dendrimers III: Design, Dimension, Function*; Springer2001.

(49) Tamam, L.; Pontoni, D.; Sapir, Z.; Yefet, S.; Sloutskin, E.; Ocko, B. M.; Reichert, H.; Deutsch, M. Modification of deeply buried hydrophobic interfaces by ionic surfactants. *Proceedings of the National Academy of Sciences*, **2011,** *108* (14), 5522-5525.

(50) Sloutskin, E.; Bain, C. D.; Ocko, B. M.; Deutsch, M. Surface freezing of chain molecules at the liquid-liquid and liquid-air interfaces. *Faraday Discussions*, **2005,** *129*, 339-352.

(51) Tokiwa, Y.; Sakamoto, H.; Takiue, T.; Aratono, M.; Matsubara, H. Effect of Alkane Chain Length and Counterion on the Freezing Transition of Cationic Surfactant Adsorbed Film at Alkane Mixture – Water Interfaces. *The Journal of Physical Chemistry B*, **2015,** *119* (20), 6235-6241.

TOC GRAPHIC